Investigation of the metal dusting attack on the temperature range 500–700 °C using X-ray tomography

S. Mathieu, L. Le Pivaingt, O. Ferry, M. Vilasi, A. Stuppfler, J-L. Guichard, Aurélie Vande Put, Daniel Monceau

Investigation of the metal dusting attack on the temperature range 500–700 °C using X-ray tomography

S. Mathieu [a,*], L. Le Pivaingt [a], O. Ferry [a], M. Vilasi [a], A. Stuppfler [b], J-L. Guichard [b], A. Vande Put [c], D. Monceau [c]

[a] Université de Lorraine, CNRS, IJL, F-54000 Nancy, France
[b] ICAR, 4 Rue Lavoisier, 54300 Moncel-lès-Lunéville, France
[c] CIRIMAT, ENSIACET-INPT, 4, allée Emile Monso, BP 44362, F-31030 Toulouse Cedex4, France

ARTICLE INFO

Keywords:
A. Alloy
B. Mass loss
C. Oxidation
C. Carburization

ABSTRACT

A test rig consisting of a quartz tube placed in a horizontal furnace made of five independently regulated heating zones allowed the evaluation of the metal dusting attack of a FeNiCr alloy. Fifteen samples were exposed in a temperature gradient from 504° to 704°C, 1.1 bar, to a highly carburizing atmosphere for 1500 h. Below 561 °C the high density of pits led to uniform corrosion whereas localized pits developed at higher temperatures. In depth pit growth rate raised to a maximum at 632 °C, then decreased showing that it depends both on temperature and on the carbon activity gradient.

1. Introduction

When exposed in carburizing atmosphere in the intermediate 400–800 °C temperature range, heat resistant alloys may suffer from severe attack by carbon, like metal dusting. This latter is a prominent cause of corrosion damage which leads to the local disintegration of the alloy into a dust of carbides, oxides, metallic particles and graphitic carbon [1–9]. Because it is characterized by a pit like degradation which grows with time exposure to the carbon-bearing gas, this catastrophic wastage is a severe problem because it seriously decreases the lifetime of the materials [10]. Metal dusting occurs under conditions where carbon deposition and oxide formation competed. For this reason, aluminum and/or chromium are generally added either to the alloy composition [11,12] or as coating [13–15] because they are able to develop protective alumina or chromia scales under very low oxygen potential, that have the potential to prevent the alloy from metal dusting.

The metal dusting phenomenon is characterized by an incubation period which partly depends on the protective nature of the oxide scale.

Metal dusting phenomenon involves supersaturated gas ($a_C > 1$) with respect to graphite and the presence of e.g. Fe or Ni containing phases, acting as catalysts. Thanks to their partially filled d-orbital by electrons, these metallic phases are able to achieve overlap with CO orbitals and push electron density into the anti-bonding orbital of CO [16,17], facilitating its dissociation according to the push-pull mechanism of Seip et al. [18]. The ability of a metallic phase to catalyze CO dissociation is therefore function of its d-orbital filling by electrons. Once the oxide scale fails to protect the alloy, catalysts are in contact with the supersaturated gas. The carbon released by CO dissociation diffuses within the alloy up to its saturation and then leads to the formation of carbides, and/or graphite [8]. This results in the alloy degradation and generally in the formation of pits at the locations where the oxide scale failed to protect the alloy. Pits growth rate can be very rapid as recently shown by Fabas et al. [19] who evaluated on a 800HT alloy an in depth pit growth up to 0.1 $\mu m.h^{-1}$ at 570 °C and 21 bars in a methane steam reforming atmosphere.

Multiple mechanisms were proposed to explain the metal dusting behavior for ferritic and austenitic materials [1–9,20–26]. For iron and low alloyed Fe-based materials, degradation is based on the formation of metastable cementite, and its decomposition into graphite and iron at the graphite/cementite interface [7] or its disintegration due to graphite nucleation and grow within cementite [8]. Corrosion of nickel and low alloyed Ni-based materials involves the formation of a carbon supersaturated matrix (small carbon solubility in the austenitic matrix [11, 20]) before degradation occurs either due to growth inside the alloy of graphitic sloping planes [4,27] or because of C crystallization within the Ni-matrix [25]. As for high alloyed Fe- and Ni-based materials, degradation mechanisms similar to those of low alloyed materials were proposed by some authors while others proposed more complex and diverse

* Corresponding author.
E-mail address: stephane.mathieu@univ-lorraine.fr (S. Mathieu).

https://doi.org/10.1016/j.corsci.2021.109863

Table 1
Nominal composition of CT15C alloy, in wt%.

wt%	C	Fe	Cr	Ni	Mn	Si	Mo	Nb
CT15C	0.1–0.18	bal.	19–23	30–35	0–1.5	0.5–1.25	0–0.5	0.8–1.2

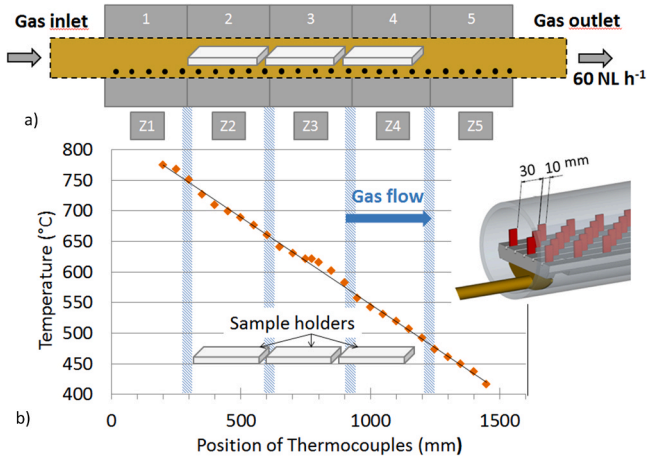

Fig. 1. a) Test rig developed for metal dusting characterization operating at 1.1 atm.; b) actual temperature gradient (in °C) along the furnace (made of five individually regulated zones); c) sample holder scheme. In this equipment, the gas flow (60 NL h^{-1}) enters the furnace from the left in the hottest zones and exits at the right. Samples were placed on the sample holders situated in the three inner zones of the furnace (Z2-Z3-Z4).

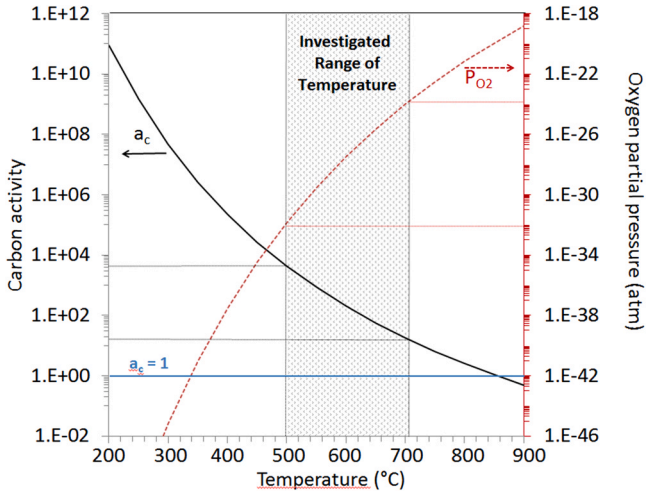

Fig. 2. Theoretical carbon activity (from Boudouard equilibrium) and oxygen partial pressure (from CO +1/2 O_2 = CO_2 equilibrium) according to the temperature. The investigated range of temperature for the present study is designated by the grey dotted area. The carbon activity and the oxygen partial pressure vary from 4×10^{3} up to 18 and from 10^{32} up to 10^{24} atm respectively.

Table 2
Thermodynamic data employed to calculate a_c and the oxygen partial pressure p (O_2) according to temperature (Fig. 2).

Reaction	ΔG° A + BT (J mol^{-1})		Ref.
	A	B	
CO + H_2 C + H_2O (Eq. 1)	-134,515	142.37	[49]
2 CO CO_2 +C (Eq. 2)	-170,700	174.5	[45]
CO + ½ O_2 CO_2 (Eq. 3)	-282,420	86.8	[50]
H_2 + ½ O_2 H_2O (Eq. 4)	-246,440	54.8	[46]

mechanisms [20,24,26].

A multiplicity of parameters, among these the temperature [28–31], the gas pressure [10,21,31–33], the nature of the atmosphere [31, 34–38], the gas velocity [39,40], the alloy composition [11,27,41–45], its microstructure [46–48] or still its surface features (cold work or surface finish [28,43]), are recognized to affect the rate of the degradation by MD [1]. In fact, the multiplicity of factors affecting metal dusting made hard the comparison of literature results. Still more complicated is the estimation of the service life of the materials basing on the available data. These are very specific to a set of conditions and generally correspond to a definite temperature that authors assumed to be the more severe for their application. A limited number of studies reports the metal dusting progression on a wide range of temperature [4, 5,10], although it is fully recognized that metal dusting occurrence strongly depends on oxide formation. Considering this difficulty and because of the specificity of the gas atmosphere which has to be tested, a test rig was specially built for the present study.

The present paper aims to present the test rig that has been developed with ICAR'partners with the overall objective to evaluate the metal dusting resistance of an austenitic heat resistant alloy (CT15C) devoted to hydrocarbon processing in a 10%H_2 – 17%N_2 – 70%CO – 3%CO_2 (in vol%) atmosphere. As components in service are rarely employed in isothermal conditions, the metal dusting behavior is assessed in the range of temperature 500–700 °C to determine the temperature domain for which the corrosion rate is the highest. X-ray tomography is systematically used to examine the attack morphology and the pit depth and diameter.

2. Materials and methods

Table 1 shows the nominal composition of the cast CT15C alloy from which the tested specimens were pulled out. The alloy presented a coarse austenitic structure with chromium and niobium rich carbides forming an eutectic network at metal grain boundaries. Grain size was between 20 and 150 μm.

The test rig consisted of a quartz tube placed in a horizontal furnace (Fig. 1a) made of five independently regulated heating zones. The regulation allowed the control of a reproducible and linear thermal gradient of approximately 3 °C per cm along the furnace length. This was checked thanks to the 27 thermocouples introduced in the tube that allow the precise measurement of the thermal gradient (Fig. 1b). The working zone was as long as 120 cm and the used temperature range for the study extended over 504–704 °C. The employed gas contained 10% H_2 – 17%N_2 – 70%CO – 3% CO_2 (in vol%) with a gas flow rate of 60 NL. h^{-1}, a gas velocity of 2.3 mm.s^{-1} and an operating total pressure of 1.1 atm.

The carbon activity (a_c) for this carbonaceous atmosphere was calculated both from CO reduction (Eq.1) and Boudouard (Eq.2) reactions, Table 2. The employed thermodynamic data are reported in Table 2. Because they are reputed to be sluggish [7], reactions involving CH_4 were not taken in account in this estimation.

In the present work, the oxygen partial pressure p(O_2) was supposed to be set by the CO/CO_2 equilibrium (Eq.3). It evolves from 10^{-32} to 10^{-24} atm between 500 °C and 700 °C. The partial pressure of water was thus deduced from the dissociation equilibrium of water (Eq.4). By the way, the carbon activity a_c can be deduced both from Eq.1 or Eq.2. The calculation showed that the carbon activity values were similar using Eq.1 or Eq.2 for this gas mixture all over the temperature range, i.e. from

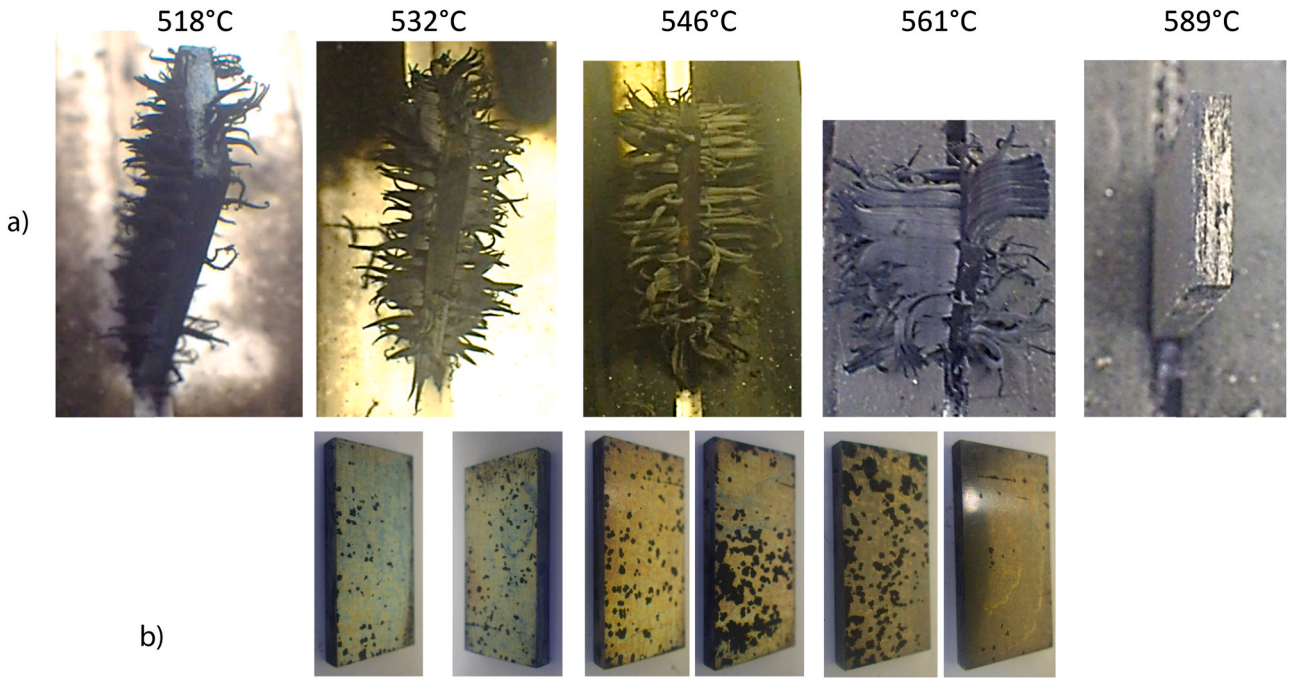

Fig. 3. Specimens observation at the 500 h intermediate stop: a) still on the sample holder (before handling) and b) both sides of the corresponding sample after cleaning (sample dimension 10 × 20 × 2 mm).

500° to 700°C.

The calculated values of a_c and $p(O_2)$ are reported in Fig. 2 for the investigated range of temperature. The carbon activity decreased with increasing temperature from 4500 to 18. These carbon activity values, greater than 1, are only possible because the carburizing atmosphere is supersaturated, i.e. not in equilibrium [8]. A mass spectrometer analyser was placed at the furnace outlet to confirm that the composition of the supersaturated gas did not change during its flow.

This out of equilibrium situation constitutes the driving force to deposit carbon. Carbon activity reaches the value of 1 at 860 °C. Therefore, at temperature higher than 860 °C, carburization could still occurs but metal dusting is not expected with the present gas mixture as the formation of graphite is not favored anymore.

In this equipment the gas enters the furnace from the left in the hottest zone and exits at the right (Fig. 1a). Samples were placed on the alumina made holders (Fig. 1c) and introduced in the inner zones of the furnace (in Z2-Z3-Z4) for experiments. Fifteen parallelepiped specimens (20 ×10 × 2 mm, i.e. a surface area of 5.2 cm^2) were introduced along the thermal gradient. Sample surface was prior ground using P800 SiC grit paper. Stops were completed at: 250 h; 500 h; 1000 h; 1250 h; 1500 h (end of run). At each stop, the furnace was cooled down at 3 °C min^{-1}. Once at room temperature, the CO containing atmosphere was replaced by argon gas. Sample holders were then removed from the furnace to characterize the specimens. The mass spectrometer analyser was used to check that the CO was fully evacuated before opening the furnace.

At in-between and final stops the samples were weighed with their adherent carbon when present at the surface. However the mass change measurement is inaccurate because of substantial carbon loss due to the specimens handling. Thus, the samples were slightly brushed to remove carbon deposit and weighed again with an accuracy of 1 mg. Only the mass variation of brushed specimens are considered in the following. Fig. 3 gives a view of the general aspect after 500 h of exposure of the samples a) still on the sample holder and b) after carbon removing. Photographs of both sides of each sample were taken at every withdrawal to follow the evolution of the corrosion damage; e.g. as shown in Fig. 3b.

As the overall mass change measurement of samples is not adapted to determine corrosion advancement for metal dusting corrosion, as it will be demonstrated hereafter, the morphology of the attack was investigated using X-ray tomography. Indeed, alloys suffering from metal dusting were degraded locally via a pitting-type mechanism. X-ray tomography allowed the full characterization of pit dimensions (diameter and depth) which were highly relevant data to determine the resistance of a given alloy to the metal dusting attack. This technique is appropriate to determine the morphology of the volume affected by corrosion because of different X-ray absorption coefficients between the alloy and the carbon rich corrosion products. Nanotom Phoenix X-ray tomograph (GE) at a spatial resolution of 11 μm/vx (vx voxel) was used to examine the samples after the final removing and cleaning (after 1500 h exposure). Samples were illuminated with a tungsten X-ray beam which allowed, using a X-photon detector, to record the beam that had passed through the sample. Image acquisition was repeated at different rotation angles and the different sections were then reconstructed using algorithms to form the three-dimensional image of the sample. Once reconstructed the evaluation of alloy wastage morphology and wastage rate were deduced from the dimensional investigation of these 3D numerical samples. It should be noticed that because of the spatial resolution of 11 μm, no attempt was performed to estimate mass variation from the X-ray tomography results.

3. Results

3.1. Mass change measurements

Fig. 4 reports the mass change measurements vs time and temperature of cleaned samples. It is chosen here to report the mass loss at each stop rather than the mass loss evolution vs time of each sample for a better emphasis of the temperature effect. Moreover, the plot of mass loss of samples is preferred to the one of mass gain because samples exhibit mass gains only for the first runs (250 h and 500 h). The mass gain testifies for CT15C oxidation during the first period. It is supposed that after sample cleaning the mass associated to residual carbon deposit is negligible. No degradation of the sample surfaces was detected after 250 h of exposure after careful observation of the samples using an optical microscope.

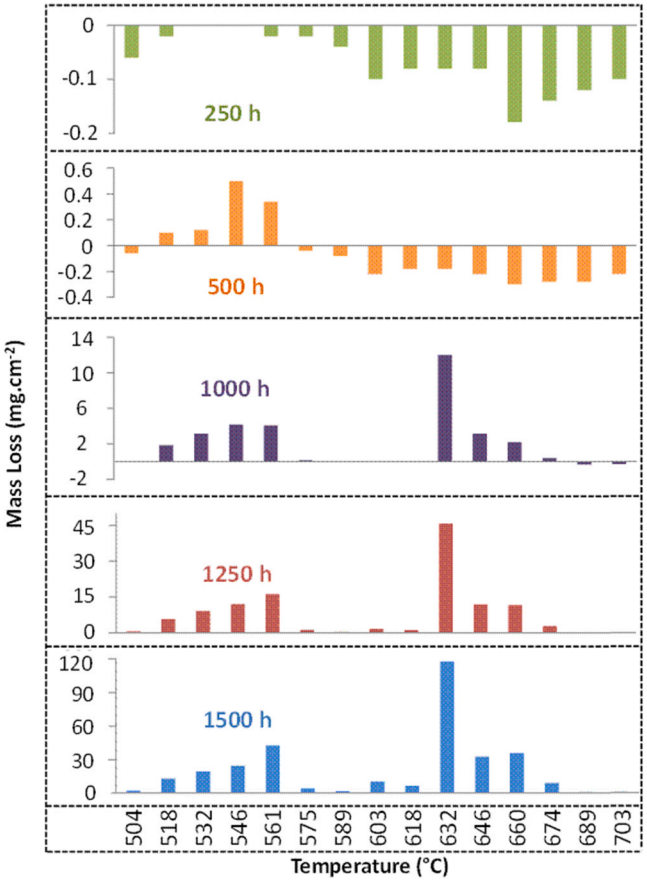

Fig. 4. Mass loss versus temperature according to the exposure time. The negative reported values have to be considered as mass gains: such situation happens when mass gain due to oxidation of alloys is larger than the metal loss due to metal dusting. Accuracy on mass change measurement was of ± 1 mg. Mass losses at 689 and 704 °C at 1250 h and 1500 h were lower than 3 mg.cm ^{2}.

After 500 h of exposure, the samples exposed to temperatures lower than 561 °C presented mass gains due to carbon deposit (not shown here) but mass loss after cleaning. Some carbon remained stuck to the surface of these samples after cleaning. At the opposite, at higher temperatures samples still presented mass gains showing that the oxidation of the alloy pursued.

After 1000 h of exposure, all samples placed in the ranges 518–575 °C and 632–674 °C were losing mass. At intermediate temperature and at the highest temperatures of 689 °C and 703 °C the mass gain still predominated.

Finally, at longer exposure time (1250 and 1500 h) mass loss was recorded for all samples but the mass losses at 504 °C, 689 °C and 704 °C were lower than 3 mg.cm^{-2}.

These observations demonstrate that the range of temperature where the metal dusting phenomenon occurs for this alloy spread over 518–674 °C. In this range, the evolution of mass loss with temperature evidences two critical temperature domains where the degradation occurred faster (around 560 °C and 630 °C) and a domain in between where the degradation appears rather low (from 575 up to 618 °C).

3.2. *Post exposure characterizations*

Fig. 5 shows the photographs of the cleaned surface (only one side is presented here) for all samples after the final removal - 1500 h - and the corresponding sample side reconstructed from X-ray tomography measurements according to the exposure temperature.

The surface area blackened by residual carbon increases from 504° to

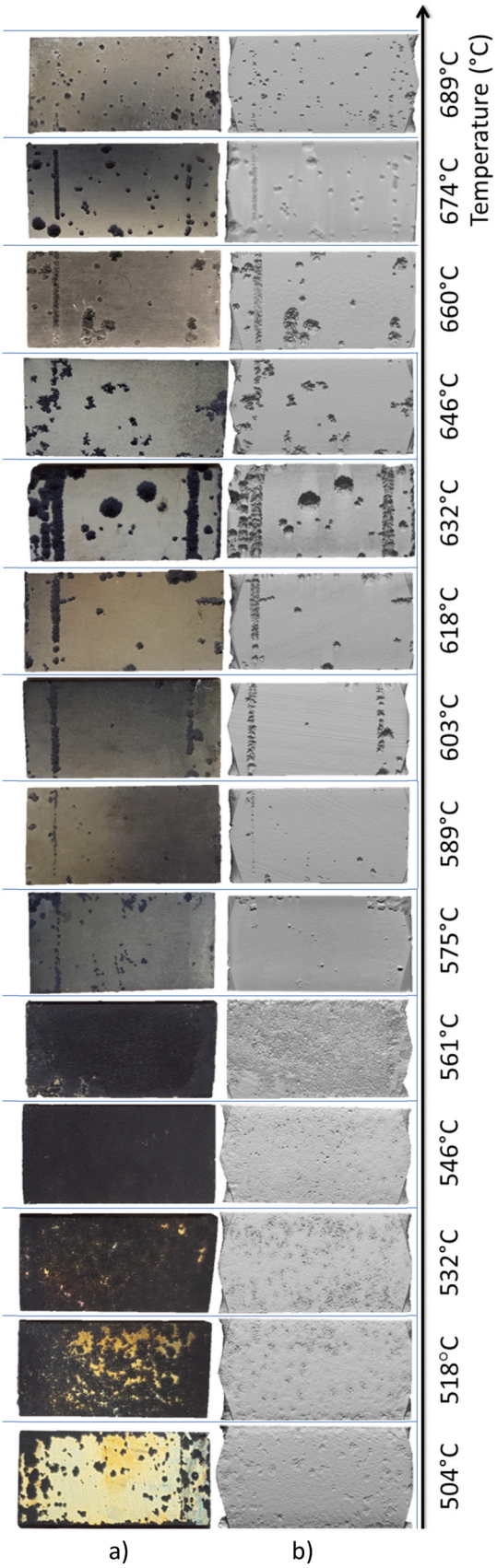

Fig. 5. a) Overall photographs of sample surface after 1500 h of exposure and b) the corresponding X-ray tomography measurements in function of the temperature. Pits lines when observed on samples have to be attributed to the neighborhood of the sample holder. (Sample dimension 10 × 20 × 2 mm).

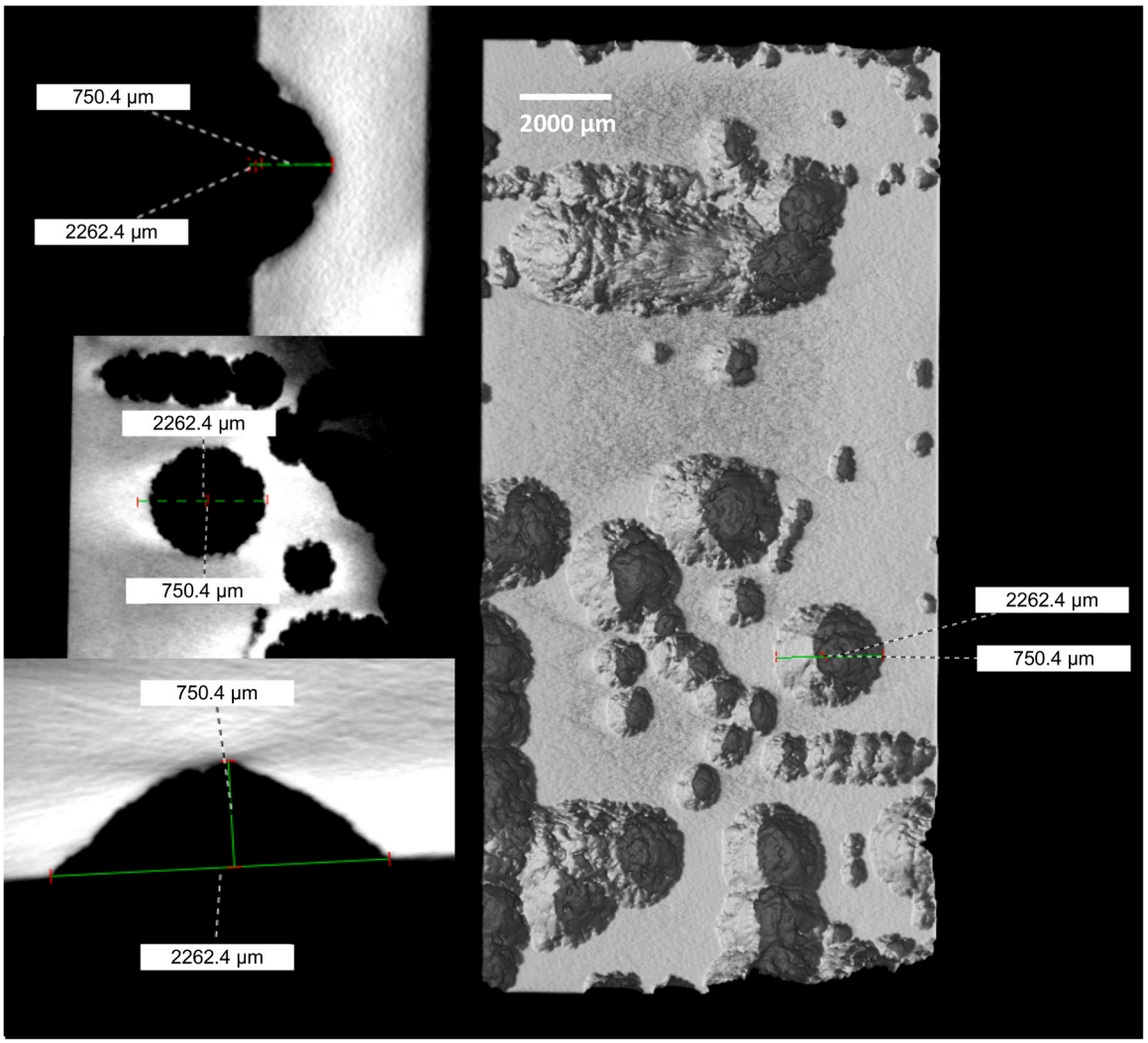

Fig. 6. Measurement procedure of pit dimensions (diameter and depth). This work was systematically done on individual pits at distance of sample edges and borders. An example of this work is reported in Appendix A and B.

561°C while the one that conserves a brightly metallic aspect decreases. Indeed, the surface of samples exposed from 504° to 532°C evidences residual bright areas while the samples at 546 and 561 °C are somewhat entirely blackened. The attack preferentially developed at edges for samples exposed at 504 and 518 °C. These observations, added to those reported in Fig. 3 for 500 h of exposure where carbon filaments developed perpendicularly to the sample surface, show that the attack occurred first at definite locations before the number of pits increased such that the attack looks generalized at the entire sample surface from 532° to 561°C. The 3D reconstructions show the surface roughness drastically increases from 504° to 561°C demonstrating that a pitting mechanism occurred for CT15C alloy in this range of temperature.

The attack morphology readily changes beyond 561 °C. The number of pits drastically decreases. The edges and the surface area that were in contact with the alumina holder are especially attacked but isolated pits are also evidenced. The latter will be very useful, particularly to determine pit growth rate as developed in Section 3.3. The location in contact with the sample holder leads to the formation of pit lines due to pit coalescence [9]. It can be noticed that this line width increases from 589 °C up to 632 °C then decreases. It is the same for the circular isolated pits for which the surface diameter follows the same trend. Pit amount and morphology can be observed using the reconstructed 3D surfaces. The number of pits per surface area has not been evaluated here because i) the number of samples is too low to have a representative statistic, ii) there is an effect of sample geometry as well as of the sample holder and iii) because this criteria does not appears as the most critical to estimate the material lifetime, as will be presented hereafter. The observation suggests their amount increases with the temperature on the range 575–689 °C but this tendency has to be taken with caution. Supplementary characterizations, of the oxide scale notably, would be necessary to definitively conclude on this trend.

Finally, if one pays attention to the diameter of the pits on the surface of a sample, the most obvious is for the sample exposed to 632 °C, it is clear that the values of the diameter of the pits do not take randomized values. Pits sizes can be classified in batches according to their diameter (Appendices A and B). A given lot corresponds to a defined nucleation date; most likely at the time of an intermediate stop.

3.3. *Exploitation of X-ray tomography results*

Fig. 6 shows the information that can be obtained from X-ray tomography reconstruction. Using these results, pit surface diameter and depth were determined measuring isolated pits at each temperature. This work was systematically done on individual pit, i.e. pit without any coalescence with surrounding pits. Moreover the individual pits were selected far from the sample edges and also far from the areas where the sample was in contact with the sample holder (e.g. pits line in Fig. 5). Pits are then classified by batches according to their dimensions as

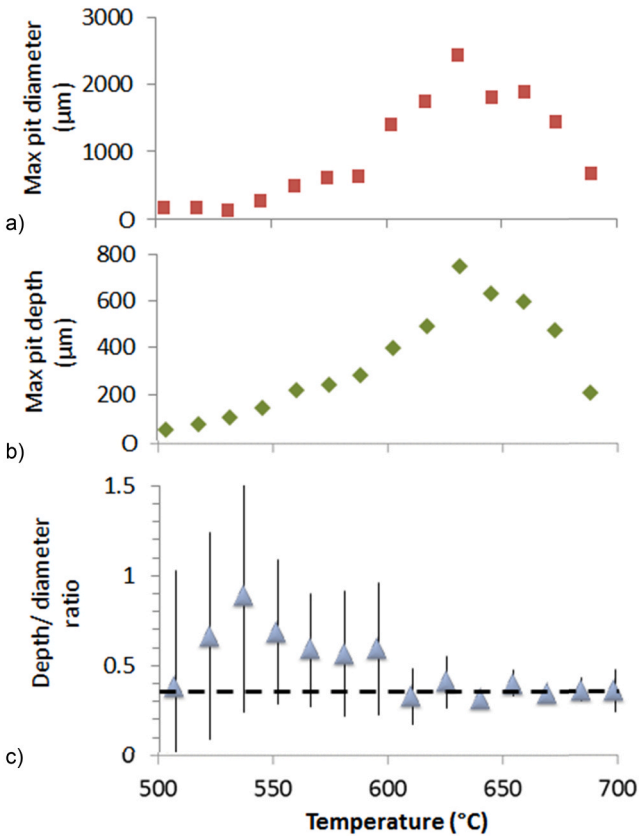

Fig. 7. a) Diameter and b) depth of the largest pit identified on each sample after 1500 h of exposure vs the exposure temperature, c) the mean depth/diameter ratio of the pits identified on each sample vs the exposure temperature (with vertical bar corresponding to standard deviation).

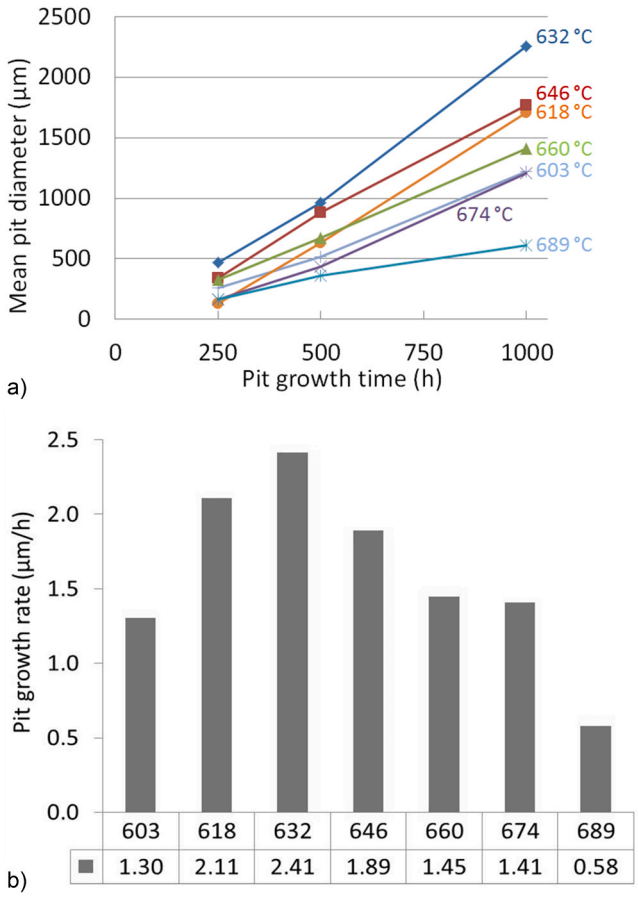

Fig. 8. a) Mean pit diameter vs pit growth time; b) lateral pit growth rate determined using the mean pit diameter vs temperature (µm.h ^{1}).

explained above (an example of this work is reported in Appendix A). The employed tomography setup gives spatial resolution of 11 µm/vx so that the smaller the size of pits, the higher is the possible error. Consequently, the measurement error below 561 °C can be high. However from 575 °C and beyond the pit growth rates are high and the error due to measurement falls down.

Results are compiled in Fig. 7, where the diameter and the depth of the largest pit identified on each sample after 1500 h of exposure vs the exposure temperature are reported. The mean depth/diameter ratio of the pits identified on each sample vs the exposure temperature (Fig. 7c) is also calculated as previously done by Natesan [20] and Fabas [19]. The number of pits that were analyzed strongly depends for each sample. It was hard to define isolated pits below 561 °C. Beneath this temperature, the measurement scattering was high, as illustrated in Fig. 7c by the standard deviation. For samples exposed between 603 and 689 °C, it was possible to estimate the dimension of more than 15 isolated pits by sample.

This treatment evidenced that the maximum pit diameter and depth increase with temperature up to 632 °C and then decrease. This trend is different of the mass measurements evolution (Fig. 4) that indicates two critical temperature ranges at which the degradation occurred faster. Using these data, it can be concluded that the critical temperature range is around 630–660 °C.

Moreover, these two parameters (pit diameter and depth) are fully correlated as demonstrated by the depth/diameter ratio evolution. For temperatures lower than 561 °C, this ratio is not really indicative because of the error made on the measurements However, from 575 °C this ratio takes a constant value of 0.35.

As indicated in Section 3.2, measurements were done on all isolated pits on both surfaces (Appendix A) and then sorted according to their size parameters (Appendix B). Putting the pictures taken at different exposure times and the pit measurements together, it is possible to estimate an initiation period for each batch of pits. According to the results, it can be deduced that pits initiate at the intermediate stops. This supposes that defects were introduced in the oxide scale during thermal cycling or sample handling. This observation is fully in agreement with the fact that the first pits were observed at the 500 h removal: i.e. pits initiated at 250 h and grew during 250 h. In Fig. 8a are reported the mean pit diameter vs the estimated growth time from crosschecking information. The results show that pit diameters evolved linearly with time for all temperatures once pits are initiated. From the latter it is extracted an estimation of the lateral pits growth rate (Fig. 8b). In agreement with mass loss (Fig. 4) and dimensional measurements (Fig. 7), the higher lateral growth rate (2.4 µm/h) was determined for the sample exposed at 632 °C.

4. Discussion

The mechanisms of metal dusting and the effect of testing conditions have been extensively studied and conversed by the past [1–5,7,8,10,12,19,22–26,41]. Some of them are still debatable and it is not the purpose of the present paper to discuss these now well-established mechanisms. The overall behavior of the austenitic CT15C alloy which contains 19–23% Cr is in fact not really different than those previously reported for NiFeCr alloys on this range of temperature. The obtained data mainly confirmed the competition that exists between the formation of a protective oxide scale and the attack by carbon as reported by Schneider et al. [4] for the Ni-15Cr alloy.

It should be first recalled that the driving force for metal dusting, i.e. the chemical potential gradient between gas and alloy, decreases as a

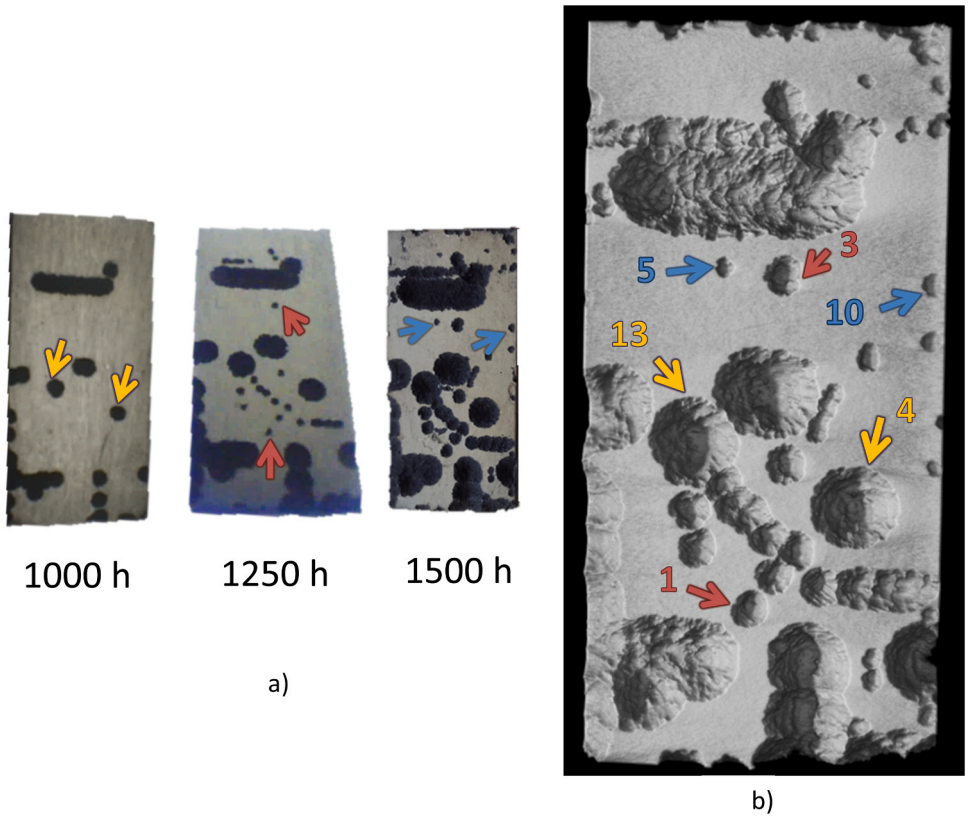

Fig. A1. a) Photographs of the sample exposed at 632 °C; b) 3D reconstructed sample after 1500 h of exposure at 632 °C. The arrows indicate the isolated pits taken in account in the data analysis.

Pit number	Diameter (µm)	Depth (µm)	Pit Initiation	Depth/diameter ratio
13	2405	747	500 h	0.31
4	2262	750		0.33
8	1117	301	1000 h	0.27
6	1005	291		0.29
3	964	314		0.33
1	937	262		0.28
7	905	257		0.28
9	870	316		0.36
14	528	180	1250 h	0.34
2	527	172		0.33
11	523	159		0.30
10	496	167		0.34
5	489	156		0.32
12	477	126		0.26

Fig. B1. Example of pit sampling made on the sample exposed at 632 °C for 1500 h.

function of temperature, as displayed by the variation of the carbon activity with temperature in Fig. 2. In opposite, the oxide growth rate as well as the kinetic of the carburization reactions, both governed by solid state diffusion, increases with temperature. As oxides scales provide diffusion barriers against carbon ingress due to their low solubility for carbon [8], a severe competition is expected on the temperature range on which protective oxide scale slowly develops and metal dusting occurs; in our case below the temperature of 860 °C for the used atmosphere.

The results evidenced the partial pressure of oxygen at equilibrium within the used carbonaceous gas was high enough to develop oxide scale at all temperatures. Indeed all specimens have gained mass - have oxidized - after the first period (250 h of exposure), Fig. 4, and all have kept at least a few areas of their surface with bright colored shades characteristic of very thin oxide scales (Figs. 3 and 5) after 1500 h of exposure, revealing these area are covered by a thin and protective oxide scale. Mass gains in relation with specimen oxidation increased with temperature, confirming the oxidation reaction is a thermally activated process.

Under the very high carbon activity range ($4500 < a_c < 18$) used for this test, all samples suffer from metal dusting on the range 504–704 °C. Nevertheless two domains can be distinguished from Fig. 5 showing the evolution of the attack vs temperature: below 561 °C and from 575 °C to 689 °C.

4.1. Metal dusting attack on the temperature range [504–561 °C]

Specimens look more or less uniformly corroded below 561 °C because of the very high number of local attack. It was more difficult to precisely determine pit parameters because of pits overlapping and because maximum pit depth didn't exceed 250 µm. This led to large discrepancy of the depth/diameter ratio over this temperature range. The pit nucleation density at low temperatures should thus be very high in comparison to higher temperatures. This finding should be in relation first with the high driving force for carbon ingress existing at low temperature, increasing nucleation sites like for precipitation reactions, and second with the oxide scale thickness and its eventual defects. In the low

temperature range, where the oxide scale is very thin (a thickness of 60–80 nm was measured on thin lamella prepared by focused ion beam on the sample exposed at 504 °C after 1500 h), it might be suggested that the diffusion length of carbon through the chromia oxide scale grain boundaries [51] can be larger than the oxide scale thickness. The handling of samples (cleaning, hand weighing, positioning on sample holder) also might in itself damage the oxide scale. Carbon ingress can, thus, occur at physical defects in the scale [8]. As a consequence the mass loss (Fig. 4) first concerns the entire surface of the sample on this temperature range and second, increases with temperature because of the increase of the diffusion rate of carbon in the alloy substrate. This constitutes the first mass loss peak of the two reported on Fig. 4.

Regardless of the metal dusting initiation mode, the results mainly showed the weakness of the oxide scale to protect the alloy from the corrosion by carbon in this low temperature range from 504° to 561°C. Further characterization of the oxide scales nature and composition would be necessary for discussing the initiation mechanism, but this does not fall in the scope of the present paper.

4.2. Metal dusting attack on the temperature range [575–689 °C]

At temperatures higher than 561 °C, the oxide layer looks to be a more efficient diffusion barrier to carbon and the attack becomes limited to local areas. The attack is no more generalized to the entire surface and as a consequence the mass loss sharply decreases.

However, one of the conclusions of the present study is also to reveal that the use of mass loss to quantify the attack by metal dusting can lead to erroneous results. Indeed if the mass gain evolution is considered only, Fig. 4, two temperature ranges where the attack is severe are obtained and in between a temperature range where the attack is very low. One could conclude that the degradation rate in the temperature range 532 – 561 °C is more or less the same as the one at 646–660 °C while the attack is rather negligible on the range 575 – 618 °C. These conclusions fall down when comparing the mass loss results to the pit depth evolution vs temperature (Fig. 7b). This latter figure shows that the pit depth continuously increases from 504° to 632°C, then decreases. This tendency is in agreement with diffusion mechanisms being activated by temperature (carbon ingress), and carbon activity evolution, the driving force for metal dusting, that decreases when temperature increases according to the CO reduction and the Boudouard reactions (Eq. 1 and 2, Table 2, Fig. 2). To the author knowledge, this is the first time it is evidenced that the in depth pit growth rate is a function of both temperature and carbon activity.

The results also evidence that on this range of temperature pit initiation has occurred, most probably during one of the intermediate stops required for weighing the samples, as observed at atmospheric pressure by Fabas et al. [20]. Cooling produces stresses in the oxide scale which can create defects such as cracks where metal dusting degradation initiates. This suggestion is sustained by two facts:

- the pit depth evolution vs exposure time follows linear kinetics (Fig. 8a). The linear regression that is obtained passes close to zero (Fig. 8a).
- no pits were observed on the samples at the 250 h intermediate stop. The first pits were observed at the 500 h intermediate stop. As the treatment of data has evidenced that the lateral pit growth rate was as high as 2.4 μm/h, no pits nucleated before the first stop. Thus it is concluded that all pits of a same batch have nucleated simultaneously, at a stop.

Therefore several authors [8,46,47,52] have previously used thermal cycling to make the metal dusting test more severe and to reduce the incubation time.

4.3. Mass change or pit density measurements vs dimensional analysis

By the past, most of the authors have quantitatively characterized metal dusting either looking at the number of pits per surface area (pit density) at a given time [10] or measuring the mass change vs time at a given temperature [1,10,12]. Nishiyama et al. [10] used a thermal gradient experiment (454–777 °C) to evaluate the corrosion by metal dusting in 24%CO–47%H_2–6%CO_2–23%H_2O for the 800 H alloy (having a composition close to the one of the CT15C alloy). They determined the number of pits per surface area to define the critical temperature range for this alloy and found 650–660 °C at P_T 40 bars and 610–620 °C at P_T 25 bars. These values are not so far from the critical temperature range observed in the present study at 1.1 bar (630–660 °C), Fig. 7b. However the authors didn't characterize the pits dimension vs temperature such that the temperature range at which the pit growth was really the fastest and the pit growth rate itself were not determined.

The present study also evidenced that the metal wastage rates in mg/cm^2/h or mm/year are valid for general attack of the entire surface; i.e. in the case of uniform degradation as previously proposed by Grabke [7]. Thus, in the present study only the corrosion rate below 561 °C, where a rather uniform degradation occurred, can be approached using mass loss. However this situation is not the most problematic for the alloy as evidenced in Fig. 7b that shows that the in depth pit growth can be very high. In fact, none of these methods, the numeration of pits per surface area (pit density) and mass loss measurements, can be used to extrapolate the in depth pit growth rate which appears to be to the present authors' point of view the most critical data to extrapolate service lifetime of materials.

4.4. In depth pit growth rate

Because the experimental determination of the pit growth rate requires many materials, precise and time consuming operations, the literature about pit growth rate is poor and the work of Fabas et al. [19] has, from this point of view, to be emphasized. Indeed these authors have proposed a modelling of the kinetics of pitting corrosion by metal dusting for the 800HT alloy at 570 °C and 21 bars. Based on the lateral pit growth rate and the observed pit depth/diameter ratio of one fifth, authors determined indirectly the pit growth rate in depth.

The highest pit growth rate in depth in their case (800HT, 570 °C, 21 bars) was around 0.09 $\mu m.h^{-1}$ [19]. Although this rate is already high for the structural materials of a methane reformer plant, it could be significantly larger if 570 °C, the temperature used in [19] to evaluate metal dusting resistance, is not the most critical temperature for 800HT alloy exposed to metal dusting under 21 bars. In fact, this temperature is low regarding the temperature at which operate parts of methane reforming equipment. It corresponds to a temperature of the equipment during the gas cooling stage. Performing exposures in a thermal gradient allows the identification of this critical temperatures range. In the present study, the highest pit growth rate in depth is obtained at the temperature of 632 °C and is equal to 0.84 $\mu m.h^{-1}$; i.e. nine to tenfold the one obtained at 570 °C, 21 bars by Fabas et al. for 800HT, an alloy with a composition not so far from the one of the present study. Of course the direct comparison between Fabas' results and the ones obtained in the present study should be done with more care as is done here because the gas pressure, the carbonaceous atmosphere and the used test rig are different. Nevertheless the comparison gives an idea of what can be missed and what can be deduced from the thermal gradient test.

4.5. Contribution of X-ray tomography to metal dusting attack measurements

The 3D X-ray tomography characterization technique used in the present study allows the evaluation of the morphology of the metal dusting attack with a reasonable accuracy. Although the resolution of

such a technique is not very high in the used conditions (11 μm/vx), it is sufficient to obtain quantitative data about pit development and metal dusting wastage. In all cases, this accuracy is lower than the errors that could be made by metallography. The 3D pit characterization evidences that pits have a spherical cap shape with a constant pit diameter/pit depth ratio at temperatures higher than 575 °C. For temperatures lower than 561 °C, this ratio is not indicative because of the error made on the measurements and also because of the number of pits; but from 575 °C the ratio takes a constant value of 0.35. This trend was also observed by [20] and [21]. The former determined a constant ratio of about 0.2 for 800HT, 601, 602CA, 617, 45TM alloys. 800HT is a Fe-based alloy and the latters are Ni-based alloys. It can be suggested that the pit morphology (pit diameter/pit depth) depends on the alloy composition and microstructure, and/or of the gas pressure. However, further experiments would be necessary to evaluate the influence of these factors on this pit depth/diameter ratio. The importance of this ratio is obvious for engineering and maintenance teams since it permits the monitoring of the internal attack of industrial tubes. Indeed if tubes surface inspection can be completed in the critical temperature range after carbon removing, using optic fiber for example, the diameter of the larger individual pits can be used to evaluate pit depth and so the residual tubes thickness.

5. Conclusions

Fifteen samples of the Ni-Fe-Cr CT15C alloy have been exposed in a temperature gradient from 500° to 700°C in a highly carburizing atmosphere. The main conclusions of this experimental work are as follow:

- All specimens suffer from metal dusting attack by pitting.
- At temperatures lower than 561 °C, the corrosion is rather uniform. This result comes from the development of a high number of pits (high pit density) causing an extensive overlapping of the pits. Nevertheless the attack is characterized by a “low” alloy recession rate. In such a case of metal dusting, mass loss measurement can be relevant to quantify the degradation.
- At higher temperatures (> 561 °C) the density of the pits is reduced and single pits develop with a regular spherical cap shape. In this case, mass loss is not relevant anymore to monitor corrosion by metal dusting and X-ray tomography succeeds in providing quantitative and practical data.
- Pits are first observed at the second stop of 500 h showing pit initiation is due to defects introduced during thermal cycling or sample handling.
- Pit growth rates are peculiarly high on the 589–689 °C range with a maximum at 632 °C for the alloy CT15C in the present condition. The attack increased up to this maximum, and decreased above, because of the opposite evolution of carbon activity and diffusion /reaction kinetics.
- The in depth pit growth rate has been shown to be a non-monotonous function of temperature, with a maximum at intermediate temperature. The in depth pit growth rate is thus considered to be both a function of the temperature and of the carbon activity.
- The pit diameter/pit depth ratio is 0.35 for this alloy in this temperature and carbon activity range. Further investigations are required to evaluate the effect of the alloy microstructure.

The metal dusting experiments carried out with a large thermal gradient, as was done in the present study, are relevant for the determination of all the morphologies of carbon attacks. They make it possible to identify the most critical cases and conditions for a given alloy in a given atmosphere. When the spatial resolution of the X-ray tomography is compatible with the size of the degradation, this technique is relevant. It makes it possible to characterize the damage in 3D at each stop. Conventional metallographic techniques do not allow this non-destructive analysis.

Funding

ADEME provided financial support for the conduct of the research.

CRediT authorship contribution statement

S. Mathieu: Methodology, Conceptualization, Formal Analysis, Validation, Data computation, Writing- original draft. **L. Le Pivaingt:** Methodology, Investigation, Data computation. **O. Ferry**: Investigation. **M. Vilasi**: Data computation, Writing- review & editing. **A. Stuppfler**: Methodology, Investigation. **J-L. Guichard**: Conceptualization, Methodology, Investigation. **A. Vande-Put:** Validation, Writing- review & editing. **D. Monceau:** Validation, Writing-review & editing.

Declaration of Competing Interest

The authors declare that they have no known competing financial interests or personal relationships that could have appeared to influence the work reported in this paper.

Data Availability

The raw/processed data required to reproduce these findings cannot be shared at this time due to technical or time limitations. Data of the present study will be made available on demand.

Acknowledgments

We are pleased to acknowledge Mr. C. Morlot for his assistance with the X-ray tomography experiments. Authors would like to thank the French Environment Agency ADEME for their financial support.

Availability of data and material

The raw/processed data required to reproduce these findings cannot be easily shared at this time due to the amount of data generated by each analysis by tomography.

APPENDIX A

See Appendix Figs. A1,B1.

References

[1] H.J. Grabke, R. Krajack, J.C. Nava, On the mechanism of catastrophic carburization: metal dusting, Corros. Sci. 35 (1993) 1141–1150.
[2] H.J. Grabke, Metal dusting, Mater. Corros. 54 (2003) 736–746.
[3] J. Klower, H.J. Grabke, E.M. Muller-Lorenz, Metal dusting of Ni-based alloys, Mater. Corros. 49 (1998) 328–329.
[4] R. Schneider, E. Pippel, J. Woltersdorf, S. Strauβ, H.J. Grabke, Microprocesses of metal dusting on nickel and Ni-base alloys, J. Steel Res. 68 (1997) 326–332.
[5] C.M. Chun, J.D. Mumford, T.A. Ramanarayanan, Mechanisms of metal dusting corrosion of Iron, J. Electrochem. Soc. 149 (2002) B348–B355.
[6] C.M. Chun, G. Bhargava, T.A. Ramanarayanan, Metal dusting corrosion of nickel based alloys, J. Electrochem. Soc. 154 (2007) C231–C240.
[7] H.J. Grabke, Thermodynamics, mechanisms and kinetics of metal dusting, Mater. Corros. 49 (1998) 303–308.
[8] D.J. Young, J. Zhang, C. Geers, M. Schütze, Recent advances in understanding metal dusting: a review, Mater. Corros. 62 (2011) 7–28.
[9] D.J. Young, J. Zhang, Understanding metal dusting mechanisms, ECS Trans. 16 (44) (2009) 3–15.
[10] Y. Nishiyama, K. Kitamura, N. Otsuka, Metal dusting behaviour of Alloy 800H in laboratory carbonaceous environments under high pressure, Mater. Sci. 595–598 (2008) 649–660.
[11] Y. Nishiyama, N. Otsuka, T. Kudo, Metal dusting behaviour of Cr–Ni steels and Ni-base alloys in a simulated syngas mixture, Corros. Sci. 48 (2006) 2064–2083.
[12] D.J. Young. High Temperature Oxidation and Corrosion of Metals, Elsevier,, Oxford, 2008.
[13] C. Rosado, M. Schutze, Protective behavior of newly developed coatings against metal dusting, Mater. Corros. 54 (2003) 831–853.
[14] C.M. Chun, T.A. Ramanarayanan, Metal dusting resistant alumina forming coatings for syngas production, Corros. Sci. 51 (2009) 2770–2776.

[15] J. Alvarez, D. Melo, O. Salas, J. Oseguera, V. López, Protective coatings against metal dusting, Surf. Coat. Tech. 203 (2008) 422–426.
[16] Y. Nishiyama, K. Moriguchi, N. Otsuka, T. Kudo, Improving metal dusting resistance of. transition-metals and Ni-Cu alloys, Mater. Corros. 56 (2005) 806–813.
[17] W. Andreoni, C.M. Varma, Binding and dissociation of CO on transition-metal surfaces, Phys. Rev. B 23 (1981) 437–444.
[18] U. Seip, M.C. Tsai, K. Christmann, J. Küppers, G. Ertl, Interaction of CO with an Fe (111) surface, Surf. Sci. 139 (1984) 29–42.
[19] A. Fabas, D. Monceau, S. Doublet, A. Rouaix-Vande Put, Modelling of the kinetics of pitting corrosion by metal dusting, Corros. Sci. 98 (2015) 592–604.
[20] A. Fabas, D. Monceau, C. Josse, P. Lamesle, A. Rouaix-Vande Put, Mechanism of metal dusting corrosion by pitting of a chromia-forming alloy at atmospheric pressure and low gas velocity, Corros. Sci. 104 (2016) 204–210.
[21] K. Natesan, Z. Zeng, Development of materials resistant to metal dusting degradation, report ANL-07/30, Argonne Natl. Lab. 161 (2007).
[22] R.F. Hochman, Metal deterioration in carbon monoxide and hydrocarbons at elevated temperatures, in: Third International Congress on Metallic Corrosion, USSR, Mir, Moscow, 1966.
[23] R.F. Hochman, Catastrophic deterioration of high-temperature alloys in carbonaceous atmospheres, in: Symposium on Properties of High Temperature Alloys with Emphasis on Environmental Effects, Las Vegas, The Electrochemical Society, Nevada, 1976, pp. 715–732.
[24] P. Szakálos, Mechanisms and driving forces of metal dusting, Mater. Corros. 54 (2003) 752–762.
[25] Z. Zeng, K. Natesan, Relationship of carbon crystallization to the metal-dusting mechanism of nickel, Chem. Mater. 15 (2003) 872–878.
[26] J.Z. Albertsen, A. Grong, J.C. Walmsley, R.H. Mathiesen, W. Beek, A model for high-temperature pitting corrosion in nickel-based alloys involving internal precipitation of carbides, oxides, and graphite, Metall. Mater. Trans. A 39 (2008) 1258–1276.
[27] H.J. Grabke, E.M. Müller-Lorenz, B. Eltester, M. Lucas, D. Monceau, Resistance of 9–20%Cr-steels against metal dusting, Steel Res. 68 (1997) 179–185.
[28] C.M. Chun, T.A. Ramanarayanan, Metal-dusting corrosion of low-chromium steels, Oxid. Met. 62 (2004) 71–92.
[29] E.M. Müller-Lorenz, H.J. Grabke, Coking by metal dusting of steels, Mater. Corros. 50 (1999) 614–621.
[30] C.M. Chun, T.A. Ramanarayanan, Metal dusting corrosion of austenitic 304 stainless steel, J. Electrochem. Soc. 152 (2005) B169–B177.
[31] A. Rouaix-Vande Put, K.A. Unocic, M.P. Brady, B.A. Pint, Performance of Chromia- and Alumina-Forming Fe- and Ni-base alloys exposed to metal dusting environments: The effect of water vapor and temperature, Corros. Sci. 92 (2015) 58–68.
[32] M. Maier, J.F. Norton, P.D. Frampton, Metal dusting of 9–20%Cr steels in increased pressure environments at 560 \u0002C, Mater. Corros. 49 (1998) 330–335.
[33] T.P. Levi, N. Briggs, I.E. Minchington, C.W. Thomas, Metal dusting of type 316 stainless steel in high pressure environments between 450 \u0002C and 650 \u0002C, Mater. Corros. 53 (2002) 239–246.
[34] A. Putrevu, S.K. Varma, Z. Zeng, K. Natesan, Effect of water vapor on metal dusting behavior of ferrous alloys, TMS Lett. 3 (2006) 49–50.
[35] H.Y. Yin, J. Zhang, D.J. Young, Effect of gas composition on coking and metal dusting of 2.25Cr–1Mo steel compared with iron, Corros. Sci. 51 (2009) 2983–2993.
[36] Y. Nishiyama, T. Kudo, N. Otsuka, Effect of syngas composition on metal dusting of alloy 800H in simulated reforming gas atmospheres, Corrosion 62 (2006) 54–63.
[37] J. Zhang, A. Schneider, G. Inden, Effect of gas composition on cementite decomposition and coke formation on iron, Corros. Sci. 45 (2003) 281–299.
[38] S. Herminia Camperos Guevara, Statistical lifetime modeling of FeNiCr alloys for high temperature corrosion in waste to energy plants and metal dusting in syngas production plants, Ph D thesis, ⟨https://www.theses.fr/193521385⟩.
[39] P.L. Walker, J.F. Rakszawski, G.R. Imperial, Carbon formation from carbon monoxide-hydrogen mixtures over iron catalysts. II - rates of carbon formation, J. Phys. Chem. 63 (1959) 140–149.
[40] A. Rouaix-Vande Put, A. Fabas, S. Doublet, D. Monceau, Relevance of other parameters than carbon activity in defining the severity of a metal dusting environment, Oxid. Met. 87 (2017) 655–666.
[41] J. Zhang, D.J. Young, Coking and dusting of Fe–Ni alloys in CO–H2–H2O gas mixtures, Oxid. Met. 70 (2008) 189–211.
[42] J. Zhang, D.M.I. Cole, D.J. Young, Alloying with copper to reduce metal dusting of nickel, Mater. Corros. 56 (2005) 756–764.
[43] H.J. Grabke, R. Krajak, E.M. Müller-Lorenz, S. Strauß, Metal dusting of nickel-base alloys, Mater. Corros. 47 (1996) 495–504.
[44] S. Strauß, H.J. Grabke, Role of alloying elements in steels on metal dusting, Mater. Corros. 49 (1998) 321–327.
[45] A. Fabas, A. Rouaix-Vande Put, S. Doublet, D. Domergues, M. Salem, D. Monceau, Metal dusting corrosion of austenitic alloys at low and high pressure with the effects of Cr, Al, Nb and Cu, Corros. Sci. 123 (2017) 310–318.
[46] D.J. Young, Metal dusting reaction mechanisms, Mater. Sci. Forum 522–523 (2006) 15–26.
[47] P. Speck, D.J. Young, J. Zhang, Metal dusting of nickel–aluminium alloys, Oxid. Met. 73 (2010) 255–274.
[48] H.J. Grabke, E.M. Muller-Lorenz, S. Strauss, E. Pippel, J. Woltersdorf, Effects of grain size, cold working, and surface finish on the metal-dusting resistance of steels, Oxid. Met 50 (1998) 241–254.
[49] O. Kubaschewski, C.B. Alcock. Metallurgical Thermochemistry, 5th ed..,, Pergamon,, Oxford, 1983.
[50] I. Barin, G. Platzki, Thermochemical data of pure substances, VCH,, Weinheim, 1995.
[51] T.D. Nguyen, J.Q. Zhang, D.J. Young, Microstructures of chromia scales grown in CO_2, Mater. High Temp. 32 (1–2) (2015) 16–21.
[52] J. Zhang, D.J. Young, Effect of copper on metal dusting of austenitic stainless steels, Corros. Sci. 49 (2007) 1450–1467.